

Article

Lanthanum–Cerium-Modified Nickel Catalysts for Dry Reforming of Methane

Mahmud S. Lanre, Ahmed E. Abasaheed * , Anis H. Fakeeha , Ahmed A. Ibrahim * , Abdulrahman S. Al-Awadi, Abdulrahman bin Jumah, Fahad S. Al-Mubaddel  and Ahmed S. Al-Fatesh * 

Chemical Engineering Department, College of Engineering, King Saud University, P.O. Box 800, Riyadh 11421, Saudi Arabia; mahmudsofiu@gmail.com (M.S.L.); anishf@ksu.edu.sa (A.H.F.); alawadi@ksu.edu.sa (A.S.A.-A.); abinjumah@ksu.edu.sa (A.b.J.); falmubaddel@ksu.edu.sa (F.S.A.-M.)

* Correspondence: abasaheed@ksu.edu.sa (A.E.A.); aididwthts2011@gmail.com (A.A.I.); aalfatesh@ksu.edu.sa (A.S.A.-F.); Tel.: +966-11-467-6856 (A.E.A. & A.A.I.); +966-11-467-6859 (A.S.A.-F.)

Abstract: The catalyst $MNi_{0.9}Zr_{0.1}O_3$ ($M = La, Ce, \text{ and } Cs$) was prepared using the sol–gel preparation technique investigated for the dry reforming of methane reaction to examine activity, stability, and H_2/CO ratio. The lanthanum in the catalyst $LaNi_{0.9}Zr_{0.1}O_3$ was partially substituted for cerium and zirconium for yttrium to give $La_{0.6}Ce_{0.4}Ni_{0.9}Zr_{0.1-x}Y_xO_3$ ($x = 0.05, 0.07, \text{ and } 0.09$). The $La_{0.6}Ce_{0.4}Ni_{0.9}Zr_{0.1-x}Y_xO_3$ catalyst's activity increases with an increase in yttrium loading. The activities of the yttrium-modified catalysts $La_{0.6}Ce_{0.4}Ni_{0.9}Zr_{0.03}Y_{0.07}O_3$ and $La_{0.6}Ce_{0.4}Ni_{0.9}Zr_{0.01}Y_{0.09}O_3$ are higher than the unmodified $La_{0.6}Ce_{0.4}Ni_{0.9}Zr_{0.1}O_3$ catalyst, the latter having methane and carbon dioxide conversion values of 84% and 87%, respectively, and the former with methane and carbon dioxide conversion values of 86% and 90% for $La_{0.6}Ce_{0.4}Ni_{0.9}Zr_{0.03}Y_{0.07}O_3$ and 89% and 91% for $La_{0.6}Ce_{0.4}Ni_{0.9}Zr_{0.01}Y_{0.09}O_3$, respectively. The BET analysis depicted a low surface area of samples ranging from 2 to 9 m^2/g . The XRD peaks confirmed the formation of a monoclinic phase of zirconium. The TPR showed that apparent reduction peaks occurred in moderate temperature regions. The TGA curve showed weight loss steps in the range 773 K–973 K, with $CsNi_{0.9}Zr_{0.1}O_3$ carbon deposition being the most severe. The coke deposit on $La_{0.6}Ce_{0.4}Ni_{0.9}Zr_{0.1}O_3$ after 7 h time on stream (TOS) was the lowest, with 20% weight loss. The amount of weight loss increases with a decrease in zirconium loading.

Keywords: dry reforming of methane; catalyst activity; oxygen vacancies; carbon deposit



Citation: Lanre, M.S.; Abasaheed, A.E.; Fakeeha, A.H.; Ibrahim, A.A.; Al-Awadi, A.S.; Jumah, A.b.; Al-Mubaddel, F.S.; Al-Fatesh, A.S. Lanthanum–Cerium-Modified Nickel Catalysts for Dry Reforming of Methane. *Catalysts* **2022**, *12*, 715. <https://doi.org/10.3390/catal12070715>

Academic Editor: Maria A. Goula

Received: 1 June 2022

Accepted: 27 June 2022

Published: 29 June 2022

Publisher's Note: MDPI stays neutral with regard to jurisdictional claims in published maps and institutional affiliations.



Copyright: © 2022 by the authors. Licensee MDPI, Basel, Switzerland. This article is an open access article distributed under the terms and conditions of the Creative Commons Attribution (CC BY) license (<https://creativecommons.org/licenses/by/4.0/>).

1. Introduction

Research based on CO_2 absorption and H_2 production to solve global warming has led to the use of methane dry reforming (DRM) [1–3]. Methane dry reforming compared to partial oxidation and steam reforming in syngas generation produces a H_2/CO ratio near unity, which is appropriate for generating liquid hydrocarbons using the Fischer–Tropsch method [4–6]. The mole ratio of syngas is less than one due to side reaction; the reverse water gas shift (RWGS) step could take place in CH_4 reforming [7–9].



Hydrogen produced from greenhouse gases can decarbonize the electricity and transport sectors when substituted for fossil fuels such as coal, diesel, gasoline, and natural gas [10,11]. Due to the highly endothermic inherent features of the DRM reaction, it is performed at high temperatures (973 K–1173 K), giving rise to possible complications which affect catalyst stability and can cause the sintering of active sites [12,13].

The dry reforming of the methane reaction sequence first involves methane adsorption [14]. Generally, methane is adsorbed in a dissociated form on metals to give H and CH_x species in which the numerical value of x ranges between zero and four, which is

dependent on temperature and the metal substrate [7]. When the value of x is zero, this shows that coke is formed at the metal surface. Carbon dioxide dissociation and adsorption on transition metal are controlled by electron transfer and require the creation of an anionic CO^{2-} precursor [7]. The deactivation of catalysts by carbon formation, originating from CH_4 cracking and/or CO disproportionation (Boudouard) reaction, hinders the use of dry reforming methane.



Though noble metal catalysts such as Rh, Ru, Pt, and Pd possess good catalytic activity and better coke resistance for DRM reaction, costly prices and less availability hinder their usage [15–19]. In the dry reforming of methane, nickel-based catalysts, which are low cost, are widely used [20–23]. However, they are prone to swift deactivation due to the sintering of nickel sites and coke formation during the DRM reaction [24,25].

Perovskites are metal oxides generally represented as ABO_3 , with A and B representing the cations of two metals. The commonly used perovskites for the DRM reaction are those with Ni in the B site and A as rare-earth metals in their structure [26]. B site metal stands for the active site, whereas A site metal gives stability and augments catalytic performance [26]. The substitution of either a B or A ion with heterovalent metal ions could change the catalyst structure, generating oxygen vacancies or valence states of the original metal cation which could promote both redox properties and oxygen mobility [27]. The oxides of rare-earth metals allow for an excellent dispersion of nickel. Lanthanum shows higher stability in the DRM reaction for Ni-based catalysts [28,29]. The addition of La augments the medium-strength basicity and nickel accumulation on the catalyst surface [30]. Lanthanum was found to augment the reforming reaction by increasing the presence of NiO sites, thereby enhancing the reducibility of Ni species and carbon gasification, leading to an overall lower carbon deposit [31]. The LaNiO_3 catalyst was prepared for the steam and CO_2 reforming of methane and it was found that Ni was highly dispersed and resistant to coke deposition [32].

Ce-substituted perovskites possess enough capacity for oxygen storage and high mobility of lattice oxygen to improve catalytic behavior [33,34]. CeO_2 can create oxygen vacancies, which can eliminate carbon deposition by activating species of oxygen [34]. The ceria redox cycle between Ce^{3+} and Ce^{4+} helps to exude carbon deposited on the catalyst via oxygen vacancies [35]. Additionally, it was reported that CeO_2 can increase catalytic activity by enhancing the dispersion of surface-active components and the strong interaction between Ni and CeO_2 inhibits crystal growth [36,37]. Cesium minimizes nickel size by enhancing Ni dispersion [38]. The redox chemistry, heat stability, and oxygen-transporting capability of Zr can significantly enhance the catalytic behavior of nanocatalysts [39,40].

The objective of this research work is to evaluate the effect of the partial substitution of lanthanum in the catalyst $\text{LaNi}_{0.9}\text{Zr}_{0.1}\text{O}_3$ for cerium and zirconium for yttrium and to determine the catalytic activity and stability of each of the prepared catalysts for the CO_2 reforming of methane.

2. Results and Discussion

2.1. BET (Brunauer–Emmett–Teller) Analysis

The specific surface area of the catalysts based on the BET method range from 2 to $9 \text{ m}^2/\text{g}$ as shown in Tables 1 and 2. The specific surface area of the samples is low due to the exposure of the precursor oxides to high temperatures; this is comparable with reported values in the literature [41]. From Table 2, the increase in the amount of yttrium does not significantly affect the surface area of the catalysts. Based on the IUPAC (International Union of Pure and Applied Chemistry) classification, the hysteresis loop of $\text{CeNi}_{0.9}\text{Zr}_{0.1}\text{O}_3$ is comparable to the H3 type, as shown in Figure 1. The isotherms of yttrium-containing samples shown in Figure 2 are similar in shape and comparable to type III. The surface area

of $\text{CeNi}_{0.9}\text{Zr}_{0.1}\text{O}_3$ is slightly higher than $\text{La}_{0.6}\text{Ce}_{0.4}\text{Ni}_{0.9}\text{Zr}_{0.1}\text{O}_3$ and exhibits the highest surface area among the samples, with an isotherm comparable to type IV. The samples have particle sizes ranging from 12 to 35 nm. The isotherm curves shown in Figures 1 and 2 suggest that the materials are mesoporous with a pore diameter greater than 2 nm but less than 50 nm [40].

Table 1. Specific surface area (SSA), Pore volume (Pv), and Pore diameter (Pd) of the fresh catalyst samples.

Samples	SSA, m ² /g	Pv, cm ³ /g	Pd, nm
CsNi _{0.9} Zr _{0.1} O ₃	5.19	0.029	25.33
LaNi _{0.9} Zr _{0.1} O ₃	5.33	0.027	25.82
CeNi _{0.9} Zr _{0.1} O ₃	9.35	0.031	12.12

Table 2. Specific surface area (SSA), Pore volume (Pv) and Pore diameter (Pd) of the fresh catalyst samples.

Samples	SSA (m ² /g)	Pv (cm ³ /g)	Pd (nm)
La _{0.6} Ce _{0.4} Ni _{0.9} Zr _{0.1} O ₃	8.36	0.065	35.32
La _{0.6} Ce _{0.4} Ni _{0.9} Zr _{0.05} Y _{0.05} O ₃	3.24	0.01	16.02
La _{0.6} Ce _{0.4} Ni _{0.9} Zr _{0.03} Y _{0.07} O ₃	2.47	0.011	26.62
La _{0.6} Ce _{0.4} Ni _{0.9} Zr _{0.01} Y _{0.09} O ₃	2.64	0.011	22.43

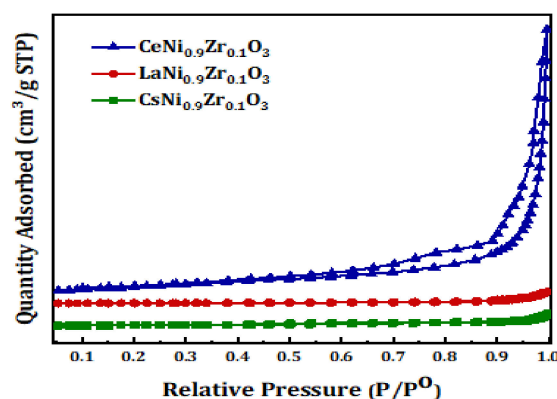


Figure 1. Nitrogen physisorption isotherms of catalyst $\text{MNi}_{0.9}\text{Zr}_{0.1}\text{O}_3$ ($M = \text{La}, \text{Ce},$ and Cs).

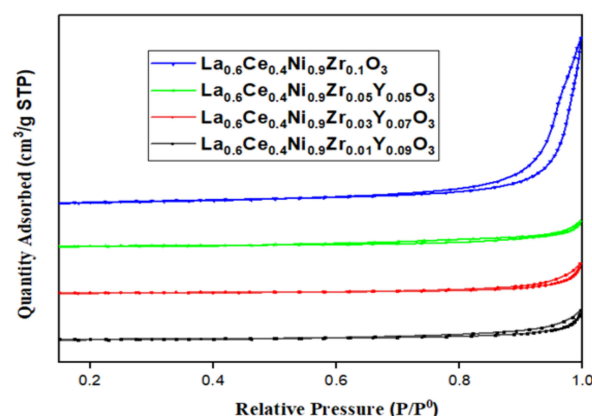


Figure 2. Nitrogen physisorption isotherms of catalyst $\text{La}_{0.6}\text{Ce}_{0.4}\text{Ni}_{0.9}\text{Zr}_{0.1-x}\text{Y}_x\text{O}_3$ ($x = 0.05, 0.07,$ and 0.09).

2.2. Temperature-Programmed Reduction (TPR)

The active sites for the catalyst $\text{MNi}_{0.9}\text{Zr}_{0.1}\text{O}_3$ ($M = \text{La}, \text{Ce},$ and Cs) samples are Ni and Zr. The reducibility was determined as shown in Figures 3 and 4. The reduction peaks are

shown in the lower and moderate temperature regions. The TPR plot suggests that there was more than one element undergoing reduction. The peaks in the moderate temperature region can be attributed to the reduction of Ni^{3+} to Ni^{2+} . Generally, the reduction becomes easier when the energy of the metal-oxygen bond decreases [41]. The cerium catalyst was reducible at lower temperatures than the lanthanum catalysts (Figure 3). The addition of yttria to lanthanum and cerium catalysts tends to move the reduction peak to the lower temperature region, with one reduction peak shown in Figure 4.

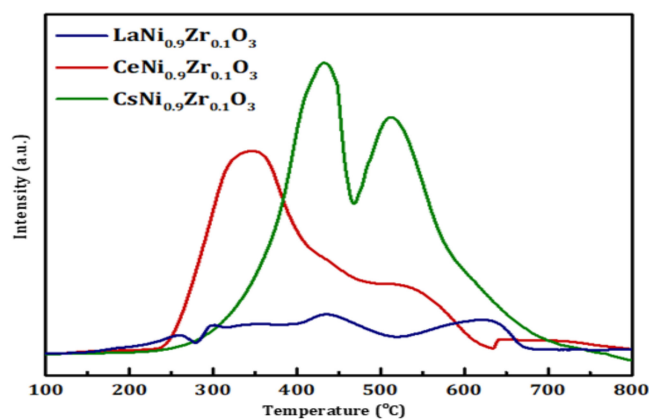


Figure 3. H_2 -TPR profiles of catalyst $\text{MNi}_{0.9}\text{Zr}_{0.1}\text{O}_3$ ($M = \text{La}, \text{Ce}, \text{and Cs}$).

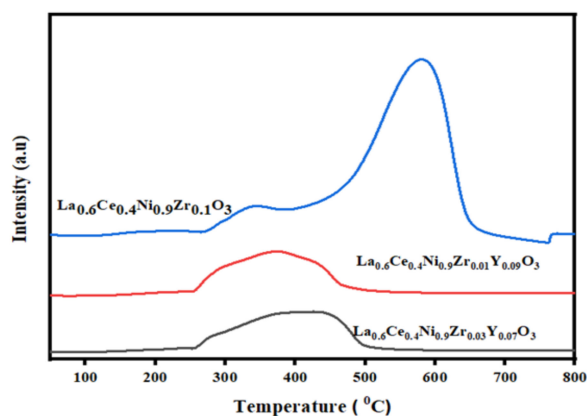


Figure 4. H_2 -TPR profiles of catalyst $\text{La}_{0.6}\text{Ce}_{0.4}\text{Ni}_{0.9}\text{Zr}_{0.1-x}\text{Y}_x\text{O}_3$ ($x = 0.05, 0.07, \text{and } 0.09$).

2.3. X-ray Diffraction (XRD) Analysis

The XRD peaks of the catalysts are depicted in Figure 5. The XRD peaks confirmed the formation of a monoclinic phase of zirconium at $2\theta = 35.3^\circ$ [41]. Peaks observed from the XRD include CeO_2 , NiO , and ZrO_2 oxides. The rhombohedral phase of LaNiO_3 (JCPDF 34-1028) is in agreement with peaks $2\theta = 23.6^\circ, 32.9^\circ, 47.3^\circ, \text{and } 60.0^\circ$ [13]. For the $\text{CeNi}_{0.9}\text{Zr}_{0.1}\text{O}_3$ catalyst, the intensity of the peaks at $2\theta = 45.2^\circ$ is higher, indicating that the substitution of La by Ce resulted in the formation of discrete crystalline phase of CeO_2 . The Ni in the Ce-Ni systems exists as NiO at the surface of the ceria and Ni^{2+} ions in the CeO_2 lattice [13].

2.4. Scanning Electron Microscope (SEM) Analysis

Figure 6 shows the SEM images of fresh $\text{MNi}_{0.9}\text{Zr}_{0.1}\text{O}_3$ ($M = \text{La}, \text{Ce}, \text{and Cs}$) catalysts. $\text{CeNi}_{0.9}\text{Zr}_{0.1}\text{O}_3$ and $\text{LaNi}_{0.9}\text{Zr}_{0.1}\text{O}_3$ catalysts appear to have irregularly shaped particles since both Ce and La belong to the same group in the periodic table. $\text{CsNi}_{0.9}\text{Zr}_{0.1}\text{O}_3$ appears to have a less coarse surface.

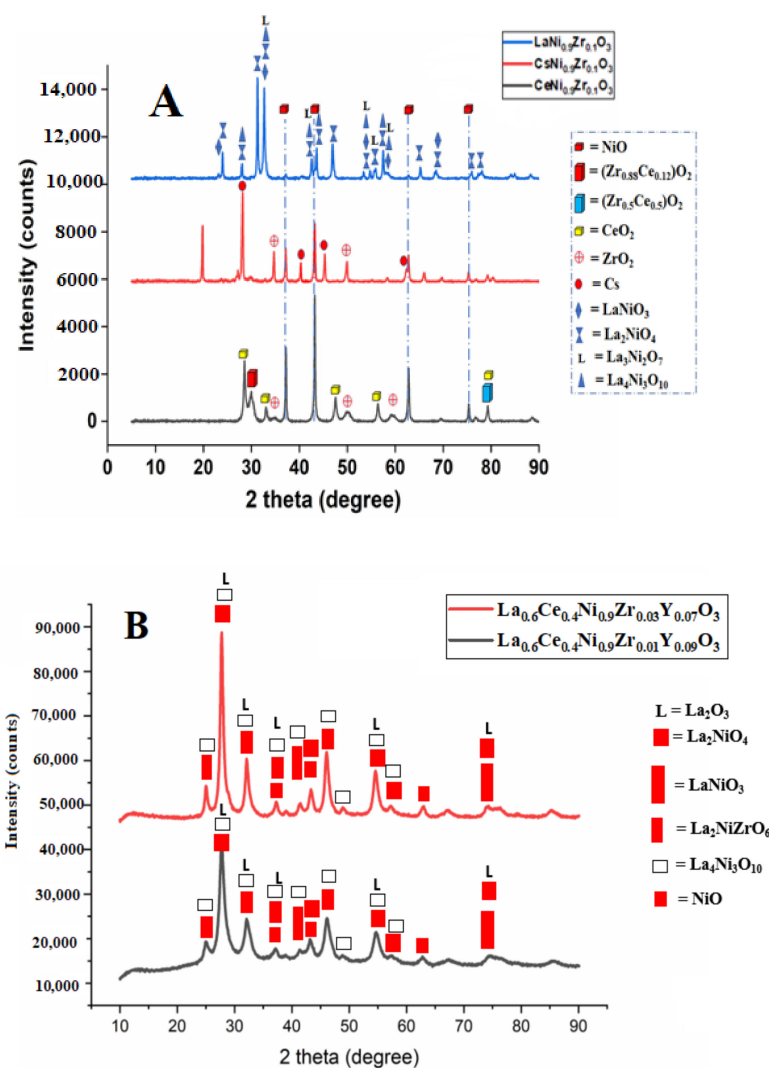


Figure 5. XRD patterns of catalyst: (A) $\text{MNi}_{0.9}\text{Zr}_{0.1}\text{O}_3$ ($M = \text{La}, \text{Ce}, \text{and Cs}$); (B) $\text{La}_{0.6}\text{Ce}_{0.4}\text{Ni}_{0.9}\text{Zr}_{0.1-x}\text{Y}_x\text{O}_3$ ($x = 0.07$ and 0.09).

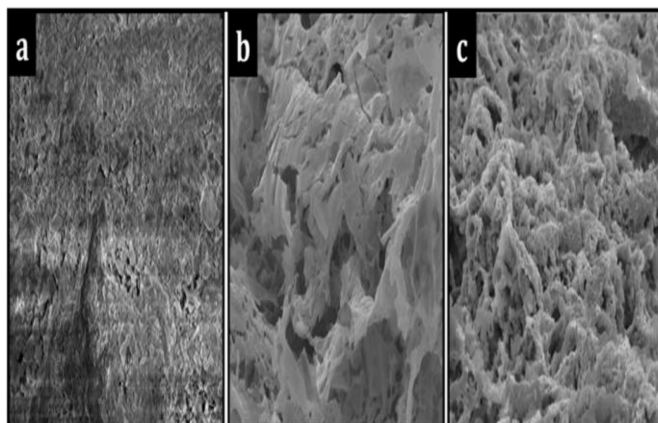


Figure 6. SEM image of fresh catalysts: (a) $\text{CsNi}_{0.9}\text{Zr}_{0.1}\text{O}_3$; (b) $\text{CeNi}_{0.9}\text{Zr}_{0.1}\text{O}_3$; (c) $\text{LaNi}_{0.9}\text{Zr}_{0.1}\text{O}_3$.

2.5. Transmission Electron Microscope (TEM) Analysis

The TEM analysis for both the fresh and spent catalysts are illustrated in Figures 7–10 at 100 and 200 nm magnifications. For the used $\text{La}_{0.6}\text{Ce}_{0.4}\text{Ni}_{0.9}\text{Zr}_{0.01}\text{Y}_{0.09}\text{O}_3$ catalyst, the particles look dispersed with the carbon aggregating on a particular spot, while for the

$\text{CeNi}_{0.9}\text{Zr}_{0.1}\text{O}_3$ catalyst, clumsy particles are shown with the carbon spreading across the surface. The nickel particle size distribution expressed in nanometers is plotted for each of the TEM images, with that of the spent catalyst higher than the fresh catalyst samples. From Table 3, the La modification of catalysts significantly reduced the crystalline nickel size from 9.44 nm to 5.68 nm, which further proves the influence of uniform Ni distribution by La, which enhances the catalyst activity.

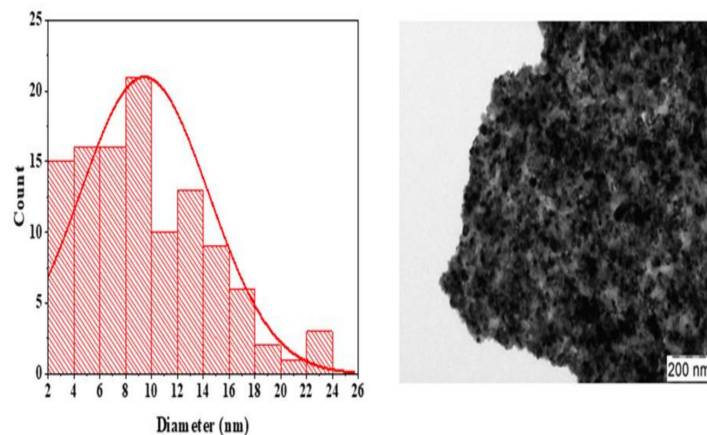


Figure 7. TEM of fresh $\text{CeNi}_{0.9}\text{Zr}_{0.1}\text{O}_3$.

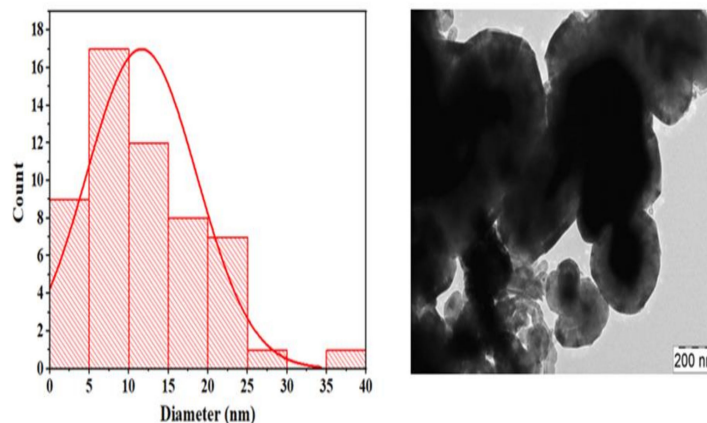


Figure 8. TEM of used $\text{CeNi}_{0.9}\text{Zr}_{0.1}\text{O}_3$.

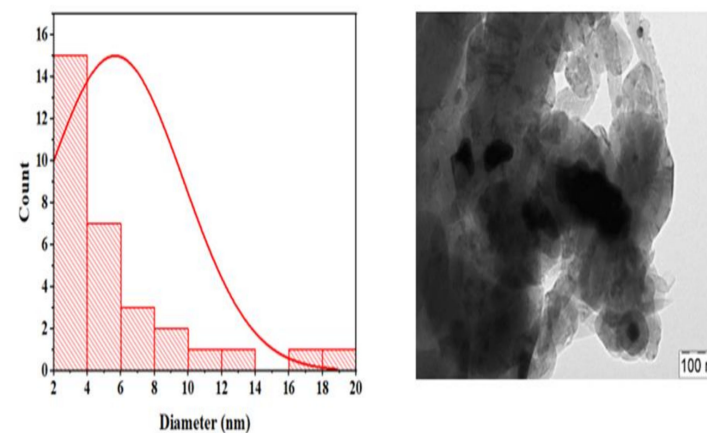


Figure 9. TEM of fresh $\text{La}_{0.6}\text{Ce}_{0.4}\text{Ni}_{0.9}\text{Zr}_{0.01}\text{Y}_{0.09}\text{O}_3$.

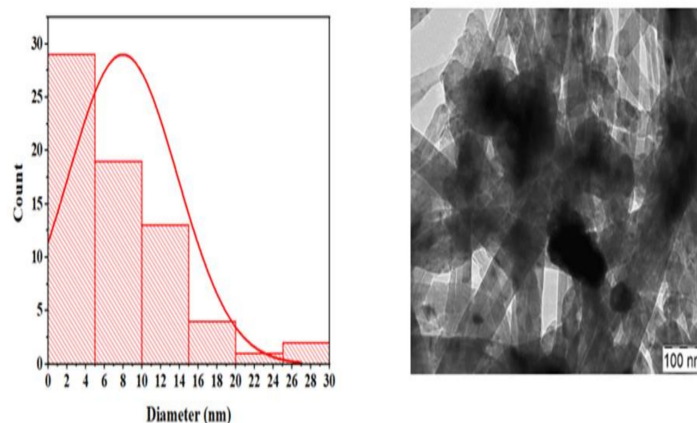


Figure 10. TEM of used $\text{La}_{0.6}\text{Ce}_{0.4}\text{Ni}_{0.9}\text{Zr}_{0.01}\text{Y}_{0.09}$.

Table 3. Nickel particle size derived from TEM analysis.

Catalyst Names	Ni Particle Size
Fresh $\text{CeNi}_{0.9}\text{Zr}_{0.1}\text{O}_3$	9.44 nm
Used $\text{CeNi}_{0.9}\text{Zr}_{0.1}\text{O}_3$	11.68 nm
Fresh $\text{La}_{0.6}\text{Ce}_{0.4}\text{Ni}_{0.9}\text{Zr}_{0.01}\text{Y}_{0.09}\text{O}_3$	5.68 nm
Used $\text{La}_{0.6}\text{Ce}_{0.4}\text{Ni}_{0.9}\text{Zr}_{0.01}\text{Y}_{0.09}\text{O}_3$	8.05 nm

2.6. Catalyst Activity

The CH_4 conversion was >75%, CO_2 conversion >85%, and H_2/CO >0.90, as shown in Figure 11 for the $\text{CeNi}_{0.9}\text{Zr}_{0.1}\text{O}_3$ catalyst. The $\text{CeNi}_{0.9}\text{Zr}_{0.1}\text{O}_3$ catalyst displayed CH_4 conversion >70%, CO_2 conversion >80%, and H_2/CO >0.90, while the $\text{LaNi}_{0.9}\text{Zr}_{0.1}\text{O}_3$ catalyst displayed CH_4 conversion >65%, CO_2 conversion >75%, and H_2/CO >0.90 for the DRM reaction performed at 1073 K for 7 hours' time on stream. CeO_2 modifies the catalytic features of nickel-based catalysts in DRM based on its redox features and enables it to support CO_2 activation ($\text{Ce}_2\text{O}_3 + \text{CO}_2 \rightarrow 2\text{CeO}_2 + \text{CO}$) [42,43]. The value of the H_2/CO ratio theoretically equals one but side reactions in the DRM experiment influence its actual value. The H_2/CO ratio values for the tested catalyst are slightly greater than one; hence, the Boudouard reaction is predominant [18]. The $\text{CeNi}_{0.9}\text{Zr}_{0.1}\text{O}_3$ catalyst shows better activity due to the abundance of oxygen vacancies, thereby creating more active sites. Studies have suggested that surface oxygen vacancy is responsible for the activation of methane. Cerium possesses a high enough capacity for oxygen storage and high mobility of lattice oxygen to improve catalytic behavior. An investigation of the influence of cerium on nickel-based catalysts for hydrogen production suggests that the addition of the right amount of cerium can increase oxygen vacancy formation, which can activate oxygen-containing compounds to react with a carbon species as soon as it forms. Lanthanum improved catalytic stability in the dry reforming of methane. The availability of La could lead to $\text{La}_2\text{O}_2\text{CO}_3$; coke deposited on the interface between Ni and $\text{La}_2\text{O}_2\text{CO}_3$ can be gasified via the reaction $\text{La}_2\text{O}_2\text{CO}_3 + \text{C} \rightarrow \text{La}_2\text{O}_3 + 2\text{CO}$. This reaction effectively suppresses coke formation on the catalyst.

A varying amount of Y was used to modify the catalyst $\text{La}_{0.6}\text{Ce}_{0.4}\text{Ni}_{0.9}\text{Zr}_{0.1}\text{O}_3$ and the reaction was carried out at 1073 K to evaluate the effect of Y loading on the modified catalyst. The $\text{La}_{0.6}\text{Ce}_{0.4}\text{Ni}_{0.9}\text{Zr}_{0.1-x}\text{Y}_x\text{O}_3$ ($x = 0.05, 0.07, \text{ and } 0.09$) catalyst's activity increases when the Y loading increases, as shown in Figure 12. The activity of $\text{La}_{0.6}\text{Ce}_{0.4}\text{Ni}_{0.9}\text{Zr}_{0.05}\text{Y}_{0.05}\text{O}_3$ is lower than the unmodified catalyst, hence the need to increase yttrium loading to 0.07 Y and 0.09 Y. The $\text{La}_{0.6}\text{Ce}_{0.4}\text{Ni}_{0.9}\text{Zr}_{0.1-x}\text{Y}_x\text{O}_3$ catalyst's activity increases with the increase in yttrium loading. The activities of the yttrium-modified catalysts $\text{La}_{0.6}\text{Ce}_{0.4}\text{Ni}_{0.9}\text{Zr}_{0.03}\text{Y}_{0.07}\text{O}_3$ and $\text{La}_{0.6}\text{Ce}_{0.4}\text{Ni}_{0.9}\text{Zr}_{0.01}\text{Y}_{0.09}\text{O}_3$ are higher than the unmodified $\text{La}_{0.6}\text{Ce}_{0.4}\text{Ni}_{0.9}\text{Zr}_{0.1}\text{O}_3$ catalyst, with the latter having methane and carbon dioxide conversion values of 84% and 87%,

respectively, and the former having methane and carbon dioxide conversion values of 86% and 90% for $\text{La}_{0.6}\text{Ce}_{0.4}\text{Ni}_{0.9}\text{Zr}_{0.03}\text{Y}_{0.07}\text{O}_3$ and 89% and 91% for $\text{La}_{0.6}\text{Ce}_{0.4}\text{Ni}_{0.9}\text{Zr}_{0.01}\text{Y}_{0.09}\text{O}_3$, respectively. Yttrium results in the formation of oxygen vacancies that are believed to contribute to improved catalytic activity. Y_2O_3 as a basic carrier allows Ni catalyst to be easily reduced and have better activity. Yttrium led to smaller Ni crystallites and enhanced the dispersion of active sites. Furthermore, doping ceria with yttrium was reported to enhance the number of oxygen vacancies and oxygen mobility. Ions of Ce^{3+} (0.97 Å) can be replaced by Y^{3+} (1.04 Å) and form a solid solution due to their similar ionic radii. La improves the interaction between the active component and the carrier, causing the even distribution of the Ni, which can be determined from SEM/EDX analysis [44]. Cerium possesses a high enough capacity of oxygen storage and high mobility of lattice oxygen to improve catalytic behavior [45]. CeO_2 can create oxygen vacancies, which can eliminate carbon deposition by activating species of oxygen [35]. The ceria redox cycle between Ce^{3+} and Ce^{4+} helps to exude carbon deposited on the catalyst via oxygen vacancies [34]. Additionally, it was reported that CeO_2 can increase catalytic activity via enhancing the dispersion of the surface-active component and the strong interaction between Ni and CeO_2 inhibiting crystal growth [36,37]. Table 4 exhibits the results of this work compared to the literature. This table denotes the suitability of the synthesized catalysts in this process. The addition of yttria to the catalyst system enhances the activity performance as compared to previous work without yttria.

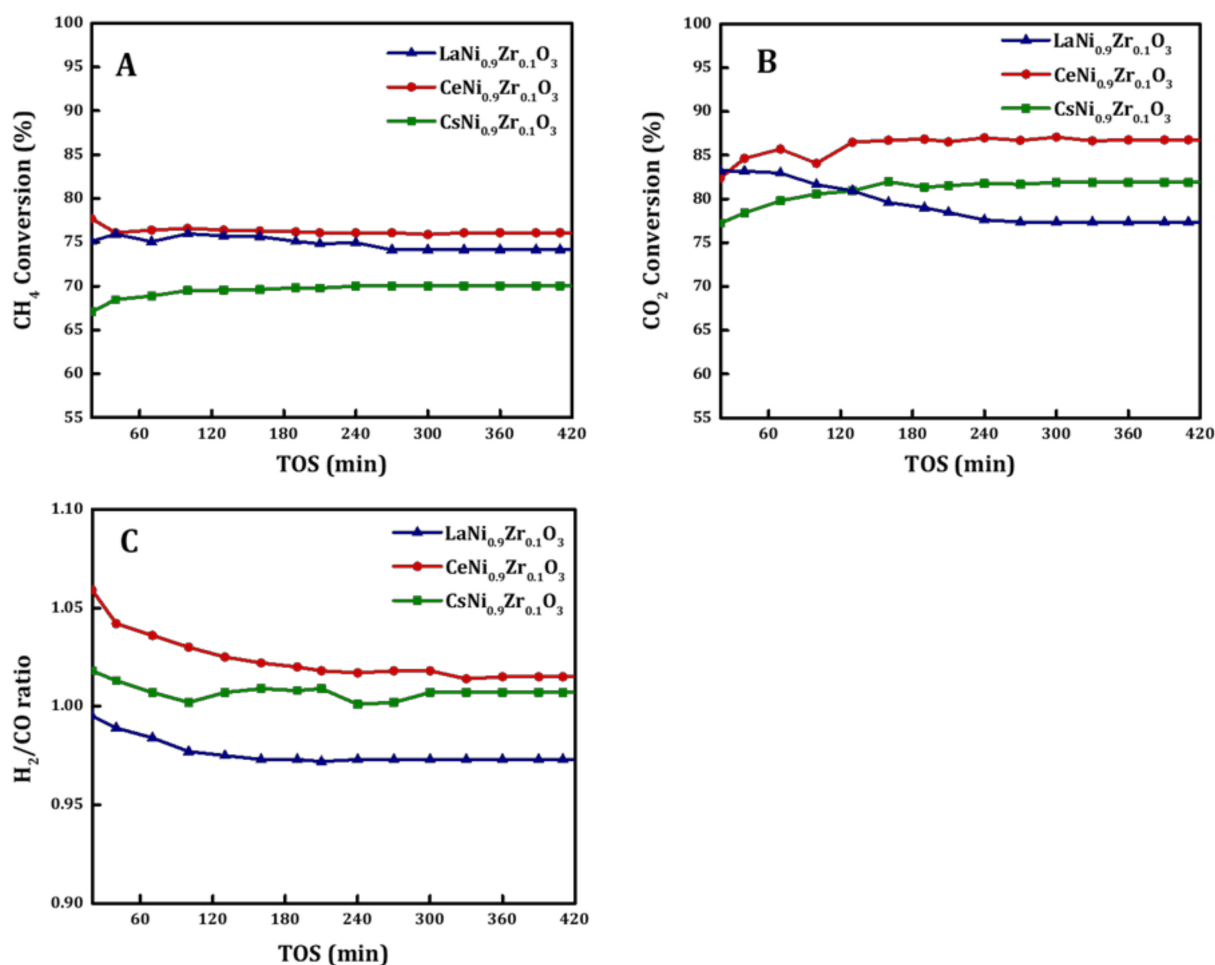


Figure 11. (A) CH_4 conversion; (B) CO_2 conversion; (C) H_2/CO ratio of catalyst $\text{MNi}_{0.9}\text{Zr}_{0.1}\text{O}_3$ ($\text{M} = \text{La}, \text{Ce}$ and Cs) at 1073 K, 1 Atmosphere and $\text{GHSV} = 42 \text{ L}/(\text{h}\cdot\text{gcat.})$.

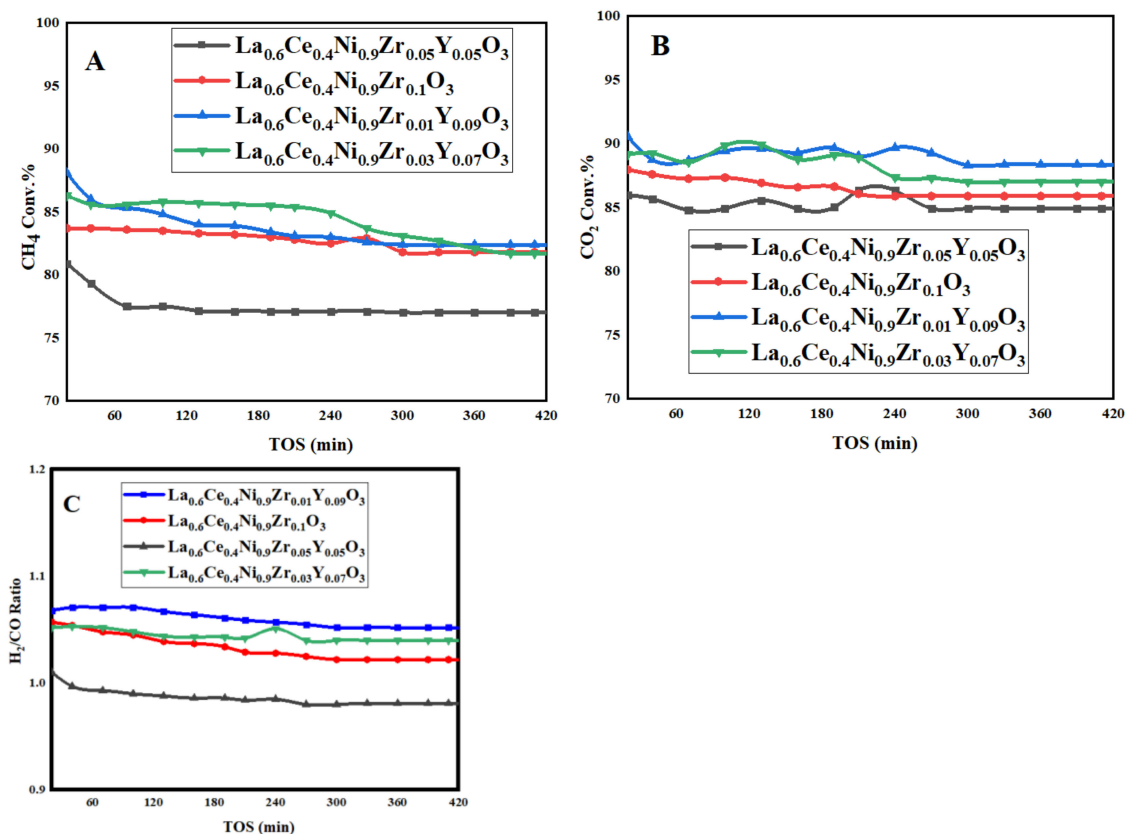


Figure 12. (A) CH₄ conversion; (B) CO₂ conversion; (C) H₂/CO ratio of catalyst La_{0.6}Ce_{0.4}Ni_{0.9}Zr_{0.1-x}Y_xO₃ (x = 0.05, 0.07, and 0.09) at 1073 K, 1 Atmosphere and GHSV = 42 L/(h·gcat.).

Table 4. Comparison of the results of this work with those of the literature.

Catalyst Constituents	Operating Temperature	Product/Conversion	Ref.
La _{0.95} Ce _{0.05} NiO ₃	1023 K	CH ₄ = 50 CO ₂ = 60	[36]
La _{0.6} Ce _{0.4} NiO ₃	1023 K	CH ₄ = 47 CO ₂ = 58	[36]
La _{0.3} Ce _{0.7} NiO ₃	1023 K	CH ₄ = 30 CO ₂ = 36	[36]
La _{0.9} Ce _{0.1} Ni _{0.9} Zr _{0.1} O ₃	1073 K	CH ₄ = 40 CO ₂ = 60	[45]
La _{0.9} Ce _{0.1} Ni _{0.8} Zr _{0.2} O ₃	1073 K	CH ₄ = 60 CO ₂ = 80	[45]
La _{0.9} Ce _{0.1} Ni _{0.7} Zr _{0.3} O ₃	1073 K	CH ₄ = 10 CO ₂ = 20	[45]
La _{0.6} Ce _{0.4} Ni _{0.9} Zr _{0.1} O ₃	1073 K	CH ₄ = 84 CO ₂ = 87	[this work]
La _{0.6} Ce _{0.4} Ni _{0.9} Zr _{0.05} Y _{0.05} O ₃	1073 K	CH ₄ = 80 CO ₂ = 85	[this work]
La _{0.6} Ce _{0.4} Ni _{0.9} Zr _{0.03} Y _{0.07} O ₃	1073 K	CH ₄ = 86 CO ₂ = 90	[this work]
La _{0.6} Ce _{0.4} Ni _{0.9} Zr _{0.01} Y _{0.09} O ₃	1073 K	CH ₄ = 89 CO ₂ = 91	[this work]

2.7. Thermogravimetric Analysis of the Used Catalyst (TGA)

The amount of coke deposited on the catalysts was determined by TGA analysis after 7 h on stream, as depicted in Figure 13. The weight loss step is in the temperature range of 773 K–973 K, with the carbon deposition of $\text{CsNi}_{0.9}\text{Zr}_{0.1}\text{O}_3$ being severe. The amount of carbon deposited on the $\text{La}_{0.6}\text{Ce}_{0.4}\text{Ni}_{0.9}\text{Zr}_{0.1}\text{O}_3$ catalyst is the lowest, indicating that La improved carbon formation resistance [26]. Although, after adding La, carbon deposits exist in the form of filamentous carbon. Adding La does not only change the way carbon deposition occurs, but may also limit it to some extent [44].

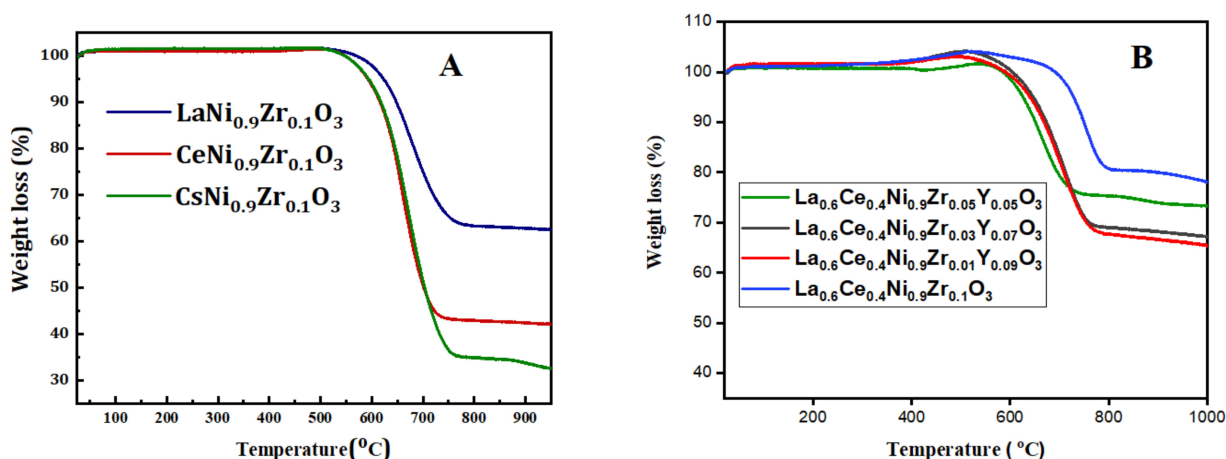


Figure 13. TGA curves of catalysts: (A) $\text{MNi}_{0.9}\text{Zr}_{0.1}\text{O}_3$ (M = La, Ce and Cs) at 1073 K; (B) $\text{La}_{0.6}\text{Ce}_{0.4}\text{Ni}_{0.9}\text{Zr}_{0.1-x}\text{Y}_x\text{O}_3$ (x = 0.05, 0.07 and 0.09).

2.8. RAMAN Analysis

Raman spectra of the used catalysts depict two bands with Raman shifts in the range of $950 \pm 5 \text{ cm}^{-1}$ and $1100 \pm 10 \text{ cm}^{-1}$, as shown in Figure 14A, and of $1574 \pm 5 \text{ cm}^{-1}$ and $2650 \pm 10 \text{ cm}^{-1}$, as shown in Figure 14B corresponding to D and G bands, respectively. The D band is related to coke deposits with imperfect or disordered structures (amorphous carbon), while the G band is a related to well-ordered structures (graphitic carbon). The value of the I_D/I_G ratio of the spent catalysts is relatively close. There is an increase in the Raman shift with the modified catalyst with yttrium.

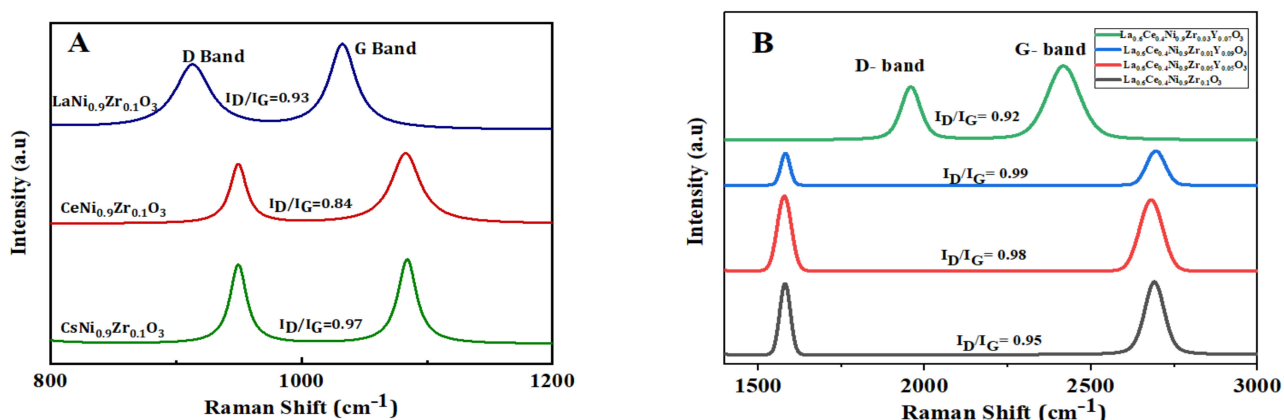


Figure 14. Raman spectra of used catalyst: (A) $\text{MNi}_{0.9}\text{Zr}_{0.1}\text{O}_3$ (M = La, Ce and Cs); (B) $\text{La}_{0.6}\text{Ce}_{0.4}\text{Ni}_{0.9}\text{Zr}_{0.1-x}\text{Y}_x\text{O}_3$ (x = 0.05, 0.07, and 0.09).

3. Experimental Section

3.1. Catalyst Preparation

The catalysts were prepared by the sol-gel method with propionic acid acting as a solvent, to dissolve nitrates of each metal. In the preparation, $\text{La}(\text{NO}_3)_3 \cdot 6\text{H}_2\text{O}$ (Sigma),

$\text{Ni}(\text{NO}_3)_2 \cdot 6\text{H}_2\text{O}$ (Sigma), $\text{Ce}(\text{NO}_3)_3 \cdot 6\text{H}_2\text{O}$ (Sigma), $\text{Cs}(\text{NO}_3)_3 \cdot 6\text{H}_2\text{O}$ (Sigma), $\text{Y}(\text{NO}_3)_3 \cdot 6\text{H}_2\text{O}$ (Sigma) $\text{ZrO}(\text{NO}_3)_2 \cdot 6\text{H}_2\text{O}$ (Sigma) and propionic acid ($\text{C}_3\text{H}_6\text{O}_2$, Sigma) were used. The nitrates were separately dissolved in propionic acid, stirred, and heated at $T = 363 \text{ K}$ with oil as a heating medium in a closed vessel. Afterward, the solutions were mixed and stirred continuously for about 2 h at $T = 403 \text{ K}$. Thereafter, the propionic acid was evaporated using a rotary evaporator at $T = 343 \text{ K}$ until a gel was formed. The gel obtained was dried at $T = 363 \text{ K}$ overnight, and calcined at 998 K for 4 h. The calcined catalysts were ground into powder and used for the DRM reaction.

3.2. Catalytic Testing

The catalysts were tested for DRM at 1073 K reaction temperature under atmospheric pressure. A packed bed stainless-steel reactor (internal diameter, 0.0091 m ; height, 0.3 m) was used to perform the experiments. A catalyst mass of 0.10 g was positioned in the reactor over a ball of glass wool. Stainless steel, sheathed thermocouple K-type, axially positioned close to the catalyst bed was used to determine the temperature during the reaction. Preceding the reaction, activation of the perovskite catalysts was achieved at 973 K in an atmosphere of H_2 . This lasted for 60 min and the remnant H_2 was purged with N_2 . During the dry reforming reaction, the feed volume ratio was kept at 3:3:1 for CH_4 , CO_2 , and N_2 gases, respectively, with a space velocity of $42 \text{ L/h} \cdot \text{gcat}$. The outlet gas from the reactor was connected to an online Gas Chromatograph (GC) with a thermal conductivity detector to analyze its composition. The CH_4 , CO_2 conversion, and H_2/CO (syngas ratio) were calculated using Equations (4)–(6):

$$\text{Methane conversion (\%)} = \frac{\text{CH}_{4,\text{in}} - \text{CH}_{4,\text{out}}}{\text{CH}_{4,\text{in}}} * 100 \quad (4)$$

$$\text{Carbon dioxide conversion (\%)} = \frac{\text{CO}_{2,\text{in}} - \text{CO}_{2,\text{out}}}{\text{CO}_{2,\text{in}}} * 100 \quad (5)$$

$$\text{Syngas Ratio} = \frac{\text{mole of H}_2 \text{ produced}}{\text{mole of CO produced}} \quad (6)$$

3.3. Determination of Catalyst's Physicochemical Properties

3.3.1. Nitrogen Physisorption

The catalyst's surface area and the pore size distribution were measured by N_2 adsorption–desorption at 77 K using a Micromeritics Tristar II 3020 for porosity and surface area analyzer.

3.3.2. Temperature Programmed Reduction (TPR) Analysis

An amount of 70 mg of the sample was loaded inside the TPR sample holder of a Micromeritics apparatus. Thereafter, TPR measurements were performed at 423 K using Ar gas for 30 min. Afterward, the sample was cooled to ambient temperature. The next step involved heating by the furnace up to 1073 K ramping at 283 K min^{-1} , in an atmosphere of H_2/Ar mixture (1:9 vol. %) flowing at 40 mL/min . The thermal conductivity unit recorded the consumption of H_2 during the operation.

3.3.3. Thermo-Gravimetric Analysis (TGA)

The quantity of carbon deposited on the spent catalysts was measured by the TG analysis. Here, a platinum pan was filled with $10\text{--}15 \text{ mg}$ of the used catalysts. Heating was carried out from room temperature up to 1273 K at 293 K min^{-1} temperature ramp. Change in mass was constantly monitored as the heating progressed.

3.3.4. X-ray Diffraction (XRD) Analysis

The X-ray Diffraction patterns of the perovskite catalysts were recorded on a Miniflex Rigaku diffractometer that was equipped with Cu K α X-ray radiation. The device was run at 40 kV and 40 mA.

3.3.5. Transmission Electron Microscopy (TEM)

Transmission electron microscopy (JEOL JEM-2100F) with high resolution to give larger magnification was used to carry out the TEM measurement of both the fresh and used catalysts. The electron microscope operated at 200 kV produces the active metal nickel particle sizes and depicts the morphology of carbon deposited on the used catalyst. Before the TEM measurement, the catalysts were first dispersed ultrasonically in ethanol at room temperature. Thereafter, the drop from the suspension was placed in a lacey carbon-coated copper grid to produce the images.

3.3.6. Laser Raman (NMR-4500) Spectrometer

Laser Raman (NMR-4500) Spectrometer (JASCO, Japan) was used to record Raman spectra of the spent catalyst samples. The wavelength of the excitation beam was set to 532 nm, and an objective lens of 100 \times magnification was used for the measurement. The laser intensity was adjusted to 1.6 mW. Each spectrum was received by averaging 3 exposures on 10 s. Spectra were recorded in the range 1200–3000 cm⁻¹ (Raman shift) and were processed by using Spectra Manager Ver.2 software (JASCO, Tokyo, Japan).

4. Conclusions

The activity of the LaNi_{0.9}Zr_{0.1}O₃ catalyst was significantly improved by partial substitution with cerium, which enhances catalyst activity due to the abundance of oxygen vacancies. The methane conversion activity of the best-modified catalyst (La_{0.6}Ce_{0.4}Ni_{0.9}Zr_{0.01}Y_{0.09}O₃) is significantly higher than the base catalyst (LaNi_{0.9}Zr_{0.1}O₃). La_{0.6}Ce_{0.4}Ni_{0.9}Zr_{0.1}O₃ activity is higher than the modified catalyst at 0.05 Y, but lower than 0.07 Y and 0.09 Y, which suggests that the activity of the modified catalyst increases above 0.05 Y. The catalyst activity increases with an increase in yttrium loading, with the La_{0.6}Ce_{0.4}Ni_{0.9}Zr_{0.01}Y_{0.09}O₃ catalyst having the best activity with a CH₄ conversion >89% and CO₂ conversion >91%. The Raman analysis suggests that carbon deposits on the catalysts are graphitic carbon. La_{0.6}Ce_{0.4}Ni_{0.9}Zr_{0.1}O₃ has the least carbon, indicating that La improved the carbon formation resistance since thermal resistance is controlled by A-cations. Furthermore, the amount of carbon deposited on the catalyst decreases with the increase in zirconium amount; hence, zirconium also enhances catalyst stability. Supplementary characterization has been explained in the Supplementary Materials.

Supplementary Materials: The following are available online at <https://www.mdpi.com/article/10.3390/catal12070715/s1>, Figure S1. The EDX analysis of fresh catalysts (A) CsNi_{0.9}Zr_{0.1}O₃ (B) CeNi_{0.9}Zr_{0.1}O₃ (C) LaNi_{0.9}Zr_{0.1}O₃; Figure S2. CO₂-TPD profiles of fresh catalysts: La_{0.6}Ce_{0.4}Ni_{0.9}Zr_{0.01}Y_{0.09}O₃ and La_{0.6}Ce_{0.4}Ni_{0.9}Zr_{0.1}O₃; Figure S3. TPO profile of used catalysts: La_{0.6}Ce_{0.4}Ni_{0.9}Zr_{0.01}Y_{0.09}O₃.

Author Contributions: Experiment, M.S.L.; writing—original draft, M.S.L. and A.S.A.-F.; preparation of the catalyst, M.S.L. and A.S.A.-F.; characterization of catalyst, M.S.L., A.S.A.-A., A.b.J. and A.A.I.; writing—review and editing, A.H.F., A.E.A., F.S.A.-M. and A.A.I. All authors have read and agreed to the published version of the manuscript.

Funding: The authors would like to sincerely thank Researchers Supporting Project number (RSP-2021/368), King Saud University, Riyadh, Saudi Arabia.

Acknowledgments: The authors would like to extend their sincere appreciation to the Researchers Supporting Project number (RSP-2021/368), King Saud University, Riyadh, Saudi Arabia.

Conflicts of Interest: The authors declare no conflict of interest.

References

1. Valderrama, G.; Kiennemann, A.; Goldwasser, M.R. La-Sr-Ni-Co-O based perovskite-type solid solutions as catalyst precursors in the CO₂ reforming of methane. *J. Power Sources* **2010**, *195*, 1765. [\[CrossRef\]](#)
2. Gallego, G.S.; Marín, J.G.; Batiot-Dupeyrat, C.; Barrault, J.; Mondragón, F. Influence of Pr and Ce in dry methane reforming catalysts produced from La_{1-x}A_xNiO_{3-δ} perovskites. *Appl. Catal. A Gen.* **2009**, *369*, 97. [\[CrossRef\]](#)
3. Steinhauer, B.; Kasireddy, M.R.; Radnik, J.; Martin, A. Development of Ni-Pd bimetallic catalysts for the utilization of carbon dioxide and methane by dry reforming. *Appl. Catal. A Gen.* **2009**, *366*, 333. [\[CrossRef\]](#)
4. Liu, H.; Wierzbicki, D.; Debek, R.; Motak, M.; Grzybek, T.; Da Costa, P.; Gálvez, M.E. La-promoted Ni-hydroxalcalite-derived catalysts for dry reforming of methane at low temperatures. *Fuel* **2016**, *182*, 8. [\[CrossRef\]](#)
5. San-José-Alonso, D.; Juan-Juan, J.; Illán-Gómez, M.J.; Román-Martínez, M.C. Ni, Co and bimetallic Ni-Co catalysts for the dry reforming of methane. *Appl. Catal. A Gen.* **2009**, *371*, 54. [\[CrossRef\]](#)
6. Hanley, E.S.; Deane, J.P.; Gallachóir, B.P.Ó. The role of hydrogen in low carbon energy futures—A review of existing perspectives. *Renew. Sustain. Energy Rev.* **2018**, *82*, 3027. [\[CrossRef\]](#)
7. Al-mubaddel, F.S.; Kumar, R.; Lanre, M.; Frusteri, F.; Aidid, A.; Kumar, V.; Olajide, S.; Hamza, A.; Elhag, A.; Osman, A.I.; et al. Optimizing acido-basic profile of support in Ni supported La₂O₃ + Al₂O₃ catalyst for dry reforming of methane. *Int. J. Hydrogen Energy* **2021**, *46*, 14225–14235. [\[CrossRef\]](#)
8. Rahmani, F.; Haghighi, M.; Vafaeian, Y.; Estifaeae, P. Hydrogen production via CO₂ reforming of methane over ZrO₂-Doped Ni/ZSM-5 nanostructured catalyst prepared by ultrasound assisted sequential impregnation method. *J. Power Sources* **2014**, *272*, 816. [\[CrossRef\]](#)
9. Zhang, L.; Wang, X.; Chen, C.; Zou, X.; Ding, W.; Lu, X. Dry reforming of methane to syngas over lanthanum-modified mesoporous nickel aluminate/γ-alumina nanocomposites by one-pot synthesis. *Int. J. Hydrogen Energy* **2017**, *42*, 11333. [\[CrossRef\]](#)
10. Al-Fatish, A.S.A.; Ibrahim, A.A.; Fakeeha, A.H.; Soliman, M.A.; Siddiqui, M.R.H.; Abasaheed, A.E. Coke formation during CO₂ reforming of CH₄ over alumina-supported nickel catalysts. *Appl. Catal. A Gen.* **2009**, *364*, 150. [\[CrossRef\]](#)
11. Itkulova, S.S.; Nurmakanov, Y.Y.; Kussanova, S.K.; Boleubayev, Y.A. Production of a hydrogen-enriched syngas by combined CO₂-steam reforming of methane over Co-based catalysts supported on alumina modified with zirconia. *Catal. Today* **2018**, *299*, 272. [\[CrossRef\]](#)
12. Sutthiumporn, K.; Maneerung, T.; Kathiraser, Y.; Kawi, S. CO₂ dry-reforming of methane over La_{0.8}Sr_{0.2}Ni_{0.8}M_{0.2}O₃ perovskite (M = Bi, Co, Cr, Cu, Fe): Roles of lattice oxygen on C–H activation and carbon suppression. *Int. J. Hydrogen Energy* **2012**, *37*, 11195. [\[CrossRef\]](#)
13. Sim, Y.; Kwon, D.; An, S.; Ha, J.M.; Oh, T.S.; Jung, J.C. Catalytic behavior of ABO₃ perovskites in the oxidative coupling of methane. *Mol. Catal.* **2020**, *489*, 110925. [\[CrossRef\]](#)
14. Kathiraser, Y.; Oemar, U.; Saw, E.T.; Li, Z.; Kawi, S. Kinetic and mechanistic aspects for CO₂ reforming of methane over Ni based catalysts. *Chem. Eng. J.* **2015**, *278*, 62. [\[CrossRef\]](#)
15. Fakeeha, A.H.; Bagabas, A.A.; Lanre, M.S.; Osman, A.I.; Elnour, A.Y.; Abasaheed, A.E.; Al-fatesh, A.S. Catalytic Performance of Metal Oxides Promoted Nickel Catalysts Supported on Mesoporous γ-Alumina in Dry Reforming of Methane. *Process* **2020**, *8*, 522. [\[CrossRef\]](#)
16. Xu, L.; Song, H.; Chou, L. Carbon dioxide reforming of methane over ordered mesoporous NiO-MgO-Al₂O₃ composite oxides. *Appl. Catal. B Environ.* **2011**, *177*, 108. [\[CrossRef\]](#)
17. Lanre, M.S.; Al-Fatesh, A.S.; Fakeeha, A.H.; Kasim, S.O.; Ibrahim, A.A.; Al-Awadi, A.S.; Al-Zahrani, A.A.; Abasaheed, A.E.; Sa, A.S.A. Catalytic Performance of Lanthanum Promoted Ni/ZrO₂ for Carbon Dioxide Reforming of Methane. *Process* **2020**, *8*, 1502. [\[CrossRef\]](#)
18. Fang, X.; Peng, C.; Peng, H.; Iu, W.; Xu, X.; Wang, X.; Li, C.; Hou, W. Methane Dry Reforming over Coke-Resistant Mesoporous Ni-Al₂O₃ Catalysts Prepared by Evaporation-Induced Self-Assembly Method. *ChemCatChem* **2015**, *7*, 3753. [\[CrossRef\]](#)
19. Patel, R.; Fakeeha, A.H.; Kasim, S.O.; Sofiu, M.L.; Ibrahim, A.A.; Abasaheed, A.E.; Kumar, R.; Al-Fatesh, A.S. Optimizing yttria-zirconia proportions in Ni supported catalyst system for H₂ production through dry reforming of methane. *Mol. Catal.* **2021**, *510*, 111676. [\[CrossRef\]](#)
20. Ewbank, J.L.; Kovarik, L.; Diallo, F.Z.; Sievers, C. Effect of metal-support interactions in Ni/Al₂O₃ catalysts with low metal loading for methane dry reforming. *Appl. Catal. A Gen.* **2015**, *494*, 57. [\[CrossRef\]](#)
21. Oemar, U.; Li Ang, M.; Hidajat, K.; Kawi, S. Enhancing performance of Ni/La₂O₃ catalyst by Sr-modification for steam reforming of toluene as model compound of biomass tar. *RSC Adv.* **2015**, *5*, 17834. [\[CrossRef\]](#)
22. Zou, X.; Wang, X.; Li, L.; Shen, K.; Lu, X.; Ding, W. Development of highly effective supported nickel catalysts for pre-reforming of liquefied petroleum gas under low steam to carbon molar ratios. *Int. J. Hydrogen Energy* **2010**, *35*, 12191. [\[CrossRef\]](#)
23. Shen, K.; Wang, X.; Zou, X.; Wang, X.; Lu, X.; Ding, W. Pre-reforming of liquefied petroleum gas over nickel catalysts supported on magnesium aluminum mixed oxides. *Int. J. Hydrogen Energy* **2011**, *36*, 4908. [\[CrossRef\]](#)
24. Råberg, L.B.; Jensen, M.B.; Olsbye, U.; Daniel, C.; Haag, S.; Mirodatos, C.; Sjøstad, A.O. Propane dry reforming to synthesis gas over Ni-based catalysts: Influence of support and operating parameters on catalyst activity and stability. *J. Catal.* **2007**, *249*, 250. [\[CrossRef\]](#)

25. Liu, D.; Quek, X.Y.; Cheo, W.N.E.; Lau, R.; Borgna, A.; Yang, Y. MCM-41 supported nickel-based bimetallic catalysts with superior stability during carbon dioxide reforming of methane: Effect of strong metal-support interaction. *J. Catal.* **2009**, *266*, 380. [[CrossRef](#)]
26. Batiot-Dupeyrat, C.; Valderrama, G.; Meneses, A.; Martinez, F.; Barrault, J.; Tatibouët, J.M. Pulse study of CO₂ reforming of methane over LaNiO₃. *Appl. Catal. A Gen.* **2003**, *248*, 143. [[CrossRef](#)]
27. Liu, Q.; Gu, F.; Lu, X.; Liu, Y.; Li, H.; Zhong, Z.; Xu, G.; Su, F. Enhanced catalytic performances of Ni/Al₂O₃ catalyst via addition of V₂O₃ for CO methanation. *Appl. Catal. A Gen.* **2014**, *488*, 37. [[CrossRef](#)]
28. Valderrama, G.; Urbina De Navarro, C.; Goldwasser, M.R. CO₂ reforming of CH₄ over Co–La-based perovskite-type catalyst precursors. *J. Power Sources* **2013**, *234*, 31. [[CrossRef](#)]
29. Ginsburg, J.M.; Piña, J.; Solh, T.; de Lasa, H.I. Coke Formation over a Nickel Catalyst under Methane Dry Reforming Conditions: Thermodynamic and Kinetic Models. *Ind. Eng. Chem. Res.* **2005**, *44*, 4846. [[CrossRef](#)]
30. Zhang, X.; Zhang, Q.; Tsubaki, N.; Tan, Y.; Han, Y. Influence of zirconia phase on the performance of Ni/ZrO₂. *Appl. Catal. A* **2015**, *34*, 135. [[CrossRef](#)]
31. Kopyscinski, J.; Schildhauer, T.J.; Biollaz, S.M.A. Production of synthetic natural gas (SNG) from coal and dry biomass—A technology review from 1950 to 2009. *Fuel* **2010**, *89*, 1763. [[CrossRef](#)]
32. Choi, S.O.; Moon, S.H. Performance of La_{1-x}Ce_xFe_{0.7}Ni_{0.3}O₃ perovskite catalysts for methane steam reforming. *Catal. Today* **2009**, *146*, 148. [[CrossRef](#)]
33. Luo, J.Z.; Yu, Z.L.; Ng, C.F.; Au, C.T. CO₂/CH₄ Reforming over Ni–La₂O₃/5A: An Investigation on Carbon Deposition and reaction steps. *J. Catal.* **2000**, *194*, 198. [[CrossRef](#)]
34. Liu, F.; Zhao, L.; Wang, H.; Bai, X.; Liu, Y. Study on the preparation of Ni–La–Ce-oxide catalyst for steam reforming of ethanol. *Int. J. Hydrogen Energy* **2014**, *39*, 10454. [[CrossRef](#)]
35. Yang, E.H.; Kim, N.Y.; Noh, Y.-S.; Lim, S.S.; Jung, J.-S.; Lee, J.S.; Hong, G.H.; Moon, D.J. Steam CO₂ reforming of methane over La_{1-x}Ce_xNiO₃ perovskite catalysts. *Int. J. Hydrogen Energy* **2015**, *40*, 11831. [[CrossRef](#)]
36. Lima, S.M.; Assaf, J.M.; Peña, M.A.; Fierro, J.L.G. Structural features of La_{1-x}Ce_xNiO₃ mixed oxides and performance for the dry reforming of methane. *Appl. Catal. A Gen.* **2006**, *311*, 94. [[CrossRef](#)]
37. Wang, Y.Z.; Li, F.M.; Cheng, H.M.; Fan, L.Y.; Zhao, Y.X. A comparative study on the catalytic properties of high Ni-loading Ni/SiO₂ and low Ni-loading Ni-Ce/SiO₂ for CO methanation. *J. Fuel Chem. Technol.* **2013**, *41*, 972. [[CrossRef](#)]
38. Frontera, P.; Candamano, M.A.; Crea, S.; Barberio, F.M.; Antonucci, P.L. Alkaline-Promoted Zeolites for Methane Dry-Reforming Catalyst Preparation. *Adv. Sci. Lett.* **2017**, *23*, 5883. [[CrossRef](#)]
39. Therdthianwong, S.; Therdthianwong, A.; Siangchin, C.; Yongprapat, S. Synthesis gas production from dry reforming of methane over Ni/Al₂O₃ stabilized by ZrO₂. *Int. J. Hydrogen Energy* **2008**, *33*, 991. [[CrossRef](#)]
40. Choque, V.; De la Piscina, P.R.; Molyneux, D.; Homs, N. Ruthenium supported on new TiO₂-ZrO₂ systems as catalysts for the partial oxidation of methane. *Catal. Today* **2010**, *149*, 248. [[CrossRef](#)]
41. Talaie, N.; Sadr, M.H.; Aghabozorg, H.; Zare, K. Synthesis and application of LaNiO₃ perovskite-type nanocatalyst with Zr for carbon dioxide reforming of methane. *Orient. J. Chem.* **2016**, *32*, 2723. [[CrossRef](#)]
42. Dama, S.; Ghodke, S.R.; Bobade, R.; Gurav, H.R.; Chilukuri, S. Active and durable alkaline earth metal substituted perovskite catalysts for dry reforming of methane. *Appl. Catal. B Environ.* **2018**, *224*, 146. [[CrossRef](#)]
43. Lanre, M.S.; Abasaeed, A.E.; Fakeeha, A.H.; Ibrahim, A.A.; Alquraini, A.A.; AlReshaidan, S.B.; Al-Fatesh, A.S. Modification of CeNi_{0.9}Zr_{0.1}O₃ Perovskite Catalyst by Partially Substituting Yttrium with Zirconia in Dry Reforming of Methane. *Materials* **2022**, *15*, 3564. [[CrossRef](#)]
44. Li, J.; Gao, R.; Zhu, L.; Zhang, Y.; Li, Z.; Li, B.; Wang, J.; He, J.; He, Y.; Qin, Z.; et al. Hydrogen-Rich Gas Production with the Ni-La/Al₂O₃-CaO-C Catalyst from Co-Pyrolysis of Straw and Polyethylene. *Catalysts* **2022**, *12*, 496. [[CrossRef](#)]
45. Dezvareha, P.; Aghabozorg, H.; Hossaini Sadrc, M.; Zared, K. Synthesis, characterization, and catalytic performance of La_{1-x}Ce_xNi_{1-y}Zr_yO₃ perovskite nanocatalysts in dry reforming of methane. *Orient. J. Chem.* **2018**, *34*, 1469–1477. [[CrossRef](#)]